

Dissecting a Small Artificial Neural Network

Xiguang Yang,¹ Krish Arora,^{1,2} and Michael Bachmann^{1,*}

¹*Soft Matter Systems Research Group, Center for Simulational Physics,
Department of Physics and Astronomy, The University of Georgia, Athens, GA 30602, USA*

²*College of Computing, Georgia Tech, Atlanta, GA 30332, USA*

We investigate the loss landscape and backpropagation dynamics of convergence for the simplest possible artificial neural network representing the logical exclusive-OR (XOR) gate. Cross-sections of the loss landscape in the nine-dimensional parameter space are found to exhibit distinct features, which help understand why backpropagation efficiently achieves convergence toward zero loss, whereas values of weights and biases keep drifting. Differences in shapes of cross-sections obtained by nonrandomized and randomized batches are discussed. In reference to statistical physics we introduce the microcanonical entropy as a unique quantity that allows to characterize the phase behavior of the network. Learning in neural networks can thus be thought of as an annealing process that experiences the analogue of phase transitions known from thermodynamic systems. It also reveals how the loss landscape simplifies as more hidden neurons are added to the network, eliminating entropic barriers caused by finite-size effects.

I. INTRODUCTION

For more than half a century, it has been believed that an artificial intelligence can be developed to simulate the astonishing cognition, reasoning, and memory capabilities of the human brain. The network of a large number of neural cells connected through synapses apparently enables complex thinking and problem solving by processing input and generating distinct output signals. Cascades of electric activation pulses from neuron to neuron mediate the learning and memorizing of signal patterns that accomplish the process of decision making.

In simple artificial neural networks, the electric activations signals are replaced by a large matrix of weights and biases that serve as input variables for a nonlinear activation function at each neuron. Basic networks are composed of a layer of input neurons, potentially multiple layers of hidden neurons to create neural capacity, and a layer of output neurons. Learning is achieved by an efficient recursive method called backpropagation [1–4]. Besides explicit mathematical calculation and computational logical algorithms, artificial neural networks can be considered an additional class of problem-solving strategies [5].

Early attempts to employ artificial neural networks date back to the late 1950s. The first such network was the perceptron, which consisted of input and output neurons only [6]. Although the potential of neural networks was recognized early, the perceptron was too simple [7, 8]. The fact that it could not be used to represent the logical XOR gate is believed to have caused the “first AI winter” at the end of the 1960s. Even though significantly improved computational and image processing equipment and algorithmic advances lead to a renewed interest through the 1980s, actual useful applications did not develop beyond so-called expert machines

capable of only solving very specific problems. Only when the global internet made computational networking possible at a large scale, leading to the creation and storage of vast amount of data, the pressing need of processing these data forced a breakthrough in the further development of artificial intelligence in the 2010s. The large networks necessary to process these data are trained in a process called deep learning, which, however, is still based on backpropagation. A large variety of neural network architectures have been proposed to accelerate the learning process [5, 9].

Studies of the Hopfield model [10] were among the first to show the deep relationship of complexity in neural networks and disordered magnetic systems. This triggered substantial interest in the statistical physics community and culminated in a vast literature on the subject in past decades. Most studies focused on understanding the many factors that can impede the performance of the optimization or learning process, though. Limiting factors are not only the architecture of the network and the optimization strategy themselves [9, 11], but also the choice of initial conditions, input data formats, and batching.

Lesser effort has been dedicated thus far to the understanding of the geometry of the underlying state space and features of the energy or loss landscape and its generalization by means of the density of states. The latter notoriously defies analytic treatment and, therefore, only recently found increasing attention in computational studies of phase transitions in finite systems. These approaches have been proven useful in applications to problems in statistical physics [12, 13].

To further advance our understanding of the complex nature of neural networks, we also establish the relationship between the two driving forces of phase transitions, energy and entropy, and determine the microcanonical entropy. Inflection points in the entropy curve have been found to be reliable indicators for phase transitions [14], even in finite systems such as biomolecules [15].

In order to make artificial intelligence a safe assistant of humanity, it is necessary to deeply understand how artifi-

* bachmann@smsyslab.org; <https://www.smsyslab.org>

cial neural networks learn and work. Given that modern complex networks often comprise billions of neurons, it is impossible to track the learning process and function in all detail. Therefore, in this paper, we take the opposite approach and study one of the smallest possible meaningful networks that is capable of solving the XOR problem. Besides the two input neurons and the single output neuron, only one additional layer of two hidden neurons is needed. Effectively, there are nine parameters to be tuned. The simplicity enables us to perform an excessive number of tests and measurements incompressible for large networks.

Yet, the learning procedures and therefore the convergence processes are similar and should give us general insights into the actual working of an artificial neural network. Particular emphasis is dedicated to features of the loss landscape embedded into the high-dimensional parameter space. Visualizing cross-sections through the landscape yields valuable insights that may help improve the performance of the parameter optimization approach. Loss landscapes are comparable to effective potential-energy and free-energy landscapes in the spaces of relevant degrees of freedom or order parameters in physical systems [16]. Consequently, different approaches to the parameterization and study of the complexity of loss landscapes have been followed [17–20], with the purpose of better understanding the influence of the landscape shape upon the dynamics of optimization processes. In this study, we pursue a more straightforward approach and investigate features of the loss landscape impacting the dynamics of backpropagation convergence, which turns out to be surprisingly complex.

The paper is organized as follows. In Sect. II, we introduce the neural network and XOR logic studied and review the optimization by backpropagation. The results we obtained from the analysis of the convergence dynamics, the features of the loss landscape, as well as the discussion of the microcanonical entropies for networks with different numbers of hidden neurons, are presented in Sect. III. The summary in Sect. IV concludes the paper.

II. XOR NEURAL NETWORK MODEL AND OPTIMIZATION

In this study, we employ a simple artificial neural network to solve the XOR problem. The binary inputs x_1 and x_2 and the output y for all four cases are listed in Table I. It is straightforward to modify this basic gate for any other logical behavior, or to add complexity, for example by simultaneously considering multiple outputs for different logical operations. However, in order to be able to thoroughly analyze the optimization of the network in detail, we keep it as simple as possible.

Since the perceptron, even with a single hidden neuron added, is known to lack capacity to memorize the four cases [8], we add more neurons to the hidden layer. Throughout the paper, we denote the number of hidden

TABLE I. Truth table of the XOR logic.

x_1	x_2	y
0	0	0
0	1	1
1	0	1
1	1	0

neurons by n_h . The simplest network we study here now consists of two neurons in the input layer, two neurons in the single hidden layer ($n_h = 2$), and the output neuron (see Fig. 1). In total, the fully connected network has six links with a weight parameter attached to each. Hidden and output neurons are assigned a bias parameter. Thus, the optimization problem to find an approximate solution that mimics the truth table in Table I is nine-dimensional. For comparison, larger networks with up to $n_h = 18$ hidden neurons have been studied as well.

We denote the weight associated with the link that connects the j th neuron in the $(l - 1)$ th layer with the i th neuron in layer l by $w_{ij}^{(l)}$, which can be considered an element of the weight matrix $\mathbf{W}^{(l)}$. For the input layer, we set $l = 0$. In our simple network, $l = 1$ is the hidden layer and $l = 2$ the output layer. The bias assigned to the i th neuron in layer l is symbolized by $b_i^{(l)}$. It is useful to also introduce the auxiliary vector

$$\mathbf{z}^{(l)} = \mathbf{W}^{(l)} \mathbf{a}^{(l-1)} + \mathbf{b}^{(l)} \quad (1)$$

with elements

$$z_i^{(l)} = \sum_{j=1}^{n_i^{(l-1)}} w_{ij}^{(l)} a_j^{(l-1)} + b_i^{(l)}, \quad (2)$$

where $n_i^{(l-1)}$ is the number of neurons in the previous layer linked to neuron j in layer l . The variable $a_j^{(l)}$ represents the activation value of the j th neuron in layer l . To determine the activation, we employ the sigmoid function

$$a_i^{(l)} = \sigma \left(z_i^{(l)} \right), \quad l > 0, \quad (3)$$

where $\sigma(z) = 1/(1 + e^{-z})$. For the input neurons, $a_i^{(0)} \equiv x_i$. The sole purpose of introducing the activation function is to break the linearity in Eq. (2). Hence, other choices than $\sigma(z)$ are also popular, foremost the simpler ReLU (rectified linear unit) function, which is mostly used in very large networks for its computational efficiency. However, for our purpose, the sigmoid function is ideal, because the range of output values in the interval $(0, 1)$ suits binary problems well and, more importantly, the gradients to be calculated in the optimization process are well-behaved and easy to control, at least in small networks like ours. As it turns out, the sigmoid approach is more robust and requires far less fine-tuning

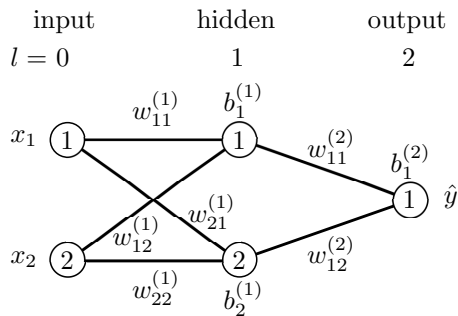


FIG. 1. Parametrization of the simplest artificial neural network used in this study with only $n_h = 2$ neurons in the hidden layer.

of control parameters such as the learning rate in the optimization process than ReLU.

Since the optimal values of the weights and biases are not known in the beginning, we set them to random values initially. Then, for a given case from Table I the activations for each neuron are calculated in the forward pass according to Eq. (3) from the input to the output side of the network. According to our setup, which does not contain a data post-processor at the output, the calculated output is simply $\hat{y} = a_1^{(2)}$.

Consequently, one learning step at given values for weights and biases contains M forward passes yielding outputs \hat{y}_m , $m = 1, \dots, M$. For our problem, a full batch consists of a set of $M = 4$ cases as this is the dimension of the input data set given in Table I. The batch can either be composed by the complete, nonrandomized sequence of all cases listed in the truth table, or the four cases are randomly chosen from the list (therefore, a case may occur more than once in a randomized batch). Both approaches were compared in our study. As the total number of cases is very small, the introduction of mini-batches is not useful here.

As a measure for the overall deviation of the calculated outputs from the true ones in the batch, we introduce the total loss function

$$L = \frac{1}{M} \sum_{m=1}^M \mathcal{L}_m, \quad (4)$$

where

$$\mathcal{L}_m = (\hat{y}_m - y_m)^2 \quad (5)$$

is the contribution to the loss from the m th case in the batch. The network performs as desired if the total loss is sufficiently close to zero.

As the complexity of neural networks prevents any analytic approach at finding the optimal weight and bias values, it is common to use a recursive approximation scheme called backpropagation [1–4]. Given that L inherently depends on all parameters, any deviation of L from zero can be traced back to deviations of weights and biases from their optimal values. Hence, following the

negative gradient of L in the space of these variables and adjusting their values accordingly should help reduce the loss in subsequent learning steps. In order to control the rate of change, it is useful to introduce the learning rate η . If we use \mathbf{v} as a generic vector, whose components v_k are all weights or biases in the nine-dimensional parameter space represented by our network, then backpropagation updates the vector \mathbf{v} from recursion (or epoch) τ to $\tau + 1$ according to

$$\mathbf{v}^{(\tau+1)} = \mathbf{v}^{(\tau)} - \eta \frac{1}{M} \sum_{m=1}^M \nabla_{\mathbf{v}} \mathcal{L}_m \left(\mathbf{v}^{(\tau)} \right), \quad (6)$$

where over the gradients, obtained from the individual cases in the batch, is averaged.

Alternative methods to optimize the network have been introduced. One such approach is zero-temperature Monte Carlo sampling [21], where the parameter values are updated randomly. If the random update of parameters leads to a lower loss, the modified parameter values are kept. Otherwise, they are reset to the values prior to the update. Currently among the most popular optimization algorithms, the Adam optimizer [22] significantly improves convergence dynamics by adaptively changing learning rates for individual parameters. We have used these methods to compare with our results obtained by standard gradient descent for the convergence dynamics. Since we concentrate here on the exploration of the geometric properties of the state space, optimizing the performance was not in the focus of this study, though.

For the estimation of the microcanonical entropy, we employed Monte Carlo sampling methods. Simple sampling, i.e., identifying states by randomly sampling the parameter space turned out to be sufficient, but results were confirmed by means of a generalized-ensemble importance-sampling method. For this purpose, we combined the Wang-Landau algorithm [23, 24] with multi-canonical sampling [16, 25, 26].

III. OPTIMIZATION CHARACTERISTICS OF THE XOR NETWORK AND LOSS LANDSCAPE

A. Dependence of Network Performance on the Learning Rate

We convinced ourselves by performing multiple long runs that the perceptron with a single hidden neuron cannot solve the problem. It does not have the necessary capacity to store the memory for all cases. The non-existence of a solution will eventually be evident from the analysis of the microcanonical entropy later. However, the addition of another hidden neuron to the neural network as shown in Fig. 1 ($n_h = 2$) is already sufficient, although the optimization process still requires a large number of epochs. Figure 2 shows the convergence of the loss function for this small network toward zero for

TABLE II. Examples of sets of optimal parameter values for the XOR network and sigmoid activation.

	$[w_{11}^{(1)}]_{\text{opt}}$	$[w_{12}^{(1)}]_{\text{opt}}$	$[w_{21}^{(1)}]_{\text{opt}}$	$[w_{22}^{(1)}]_{\text{opt}}$	$[b_1^{(1)}]_{\text{opt}}$	$[b_2^{(1)}]_{\text{opt}}$	$[w_{11}^{(2)}]_{\text{opt}}$	$[w_{12}^{(2)}]_{\text{opt}}$	$[b_1^{(2)}]_{\text{opt}}$
#1	-6.05	-6.05	-4.23	-4.24	2.36	6.29	-8.68	8.46	-3.94
#2	-6.20	5.64	5.91	-5.96	-3.78	-3.63	8.53	8.65	-3.68
#3	-6.28	-6.17	6.31	6.10	2.11	-3.28	-7.49	9.21	2.56
#4	-1.73	-8.76	1.74	9.31	-0.35	4.02	16.96	-11.51	1.02
#5	7.25	5.65	7.16	5.69	-3.25	-8.60	13.61	-14.04	-6.53

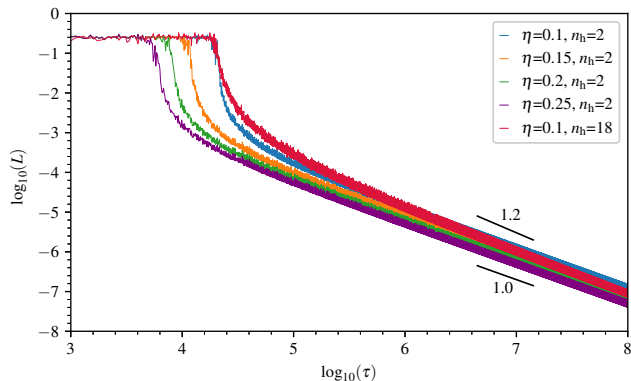


FIG. 2. Convergence of the loss function for the minimal network with $n_h = 2$ hidden neurons as a function of epochs τ for various learning rates. For comparison, the loss curve for a larger network with $n_h = 18$ neurons in the hidden layer is also included. Reference lines with values of the exponent γ attached support the power-law behavior in the long term.

multiple learning rates η . For comparison, the loss curve for a network with $n_h = 18$ neurons in the hidden layer and learning rate $\eta = 0.1$ is shown as well. Weights and biases were initialized at random values, $v_k = 0.1r_k$ ($k = 1, \dots, 9$), where $r_k \in [0, 1)$ is a random number drawn from a uniform distribution. The fluctuations are a consequence of the randomly chosen members of the batch. If the backpropagation recursions had been performed with nonrandomized batches, the curves would be smooth. As expected, the choice of the learning rate has a significant influence on the optimization dynamics. However, convergence can only be achieved within a certain range of values. For this example, in extensive tests with up to five million epochs, we found the interval of convergence to be $\eta \in [0.002, 17.484]$. For the following discussion of the optimization characteristics, we employ the results obtained for $\eta = 0.1$. Convergence sets in after about 70000 epochs. In the initial phase, the loss fluctuates about 0.25 and it seems surprising that it takes several ten thousand more epochs to complete the learning process for all cases. However, the shape of the loss landscape to be discussed later will provide essential clues.

The double-logarithmic plots in Fig. 2 offer a few particularly remarkable insights into the optimization process. Three major distinct phases of the optimization

process can be identified. First there is the initial phase, where the loss fluctuates about 0.25. This value depends on the initial parameter settings. Then there is a sudden drop into the attraction basin. In this period, the learning rate has the expected impact on the convergence dynamics. Topographically, larger learning rates make the optimization algorithm traverse the softly sloped terrain toward the basin of attraction faster. Eventually, the optimization process slows down significantly. It enters the long-term era governed by the power law

$$L(\tau) \sim \tau^{-\gamma} \quad (7)$$

with the exponent γ . For the smallest network with two hidden neurons, $\gamma \approx 1.0$, whereas its value increases to about 1.2 for the largest network studied ($n_h = 18$). Remarkably, γ does not seem to depend on the learning rate, but only on the number of hidden neurons. By comparing the networks with 2 and 18 hidden neurons at the learning rate $\eta = 0.1$, it is noteworthy that the larger network converges faster only in the long-term phase because of the larger exponent.

The optimal parameter values found with the above initialization and learning rates $\eta = 0.1$ for the network with $n_h = 2$ are listed in Table II as solution #1. This particular optimal parameter set serves as the basis for the subsequent discussion. The other examples of optimal sets of parameter values were obtained in zero-temperature Monte Carlo runs. The selection in Table II is not expected to be complete; other solutions exist. In fact, as we will see later, the space of parameter sets with marginal loss values close to zero is continuous, i.e., formally there are infinitely many parameter sets that effectively solve the problem.

B. Convergence Dynamics

A particularly striking feature in the optimization process of sigmoid neurons in this configuration of the network is that zero loss cannot be reached in a finite number of epochs. In fact, as Fig. 3 shows, the values of weights and biases keep drifting as backpropagation proceeds epoch by epoch. It poses the interesting question in how far the truncation point of the optimization dynamics impacts the performance of the network for data the network was not trained for (which cannot be verified for the logical problem in this study). From the curves for

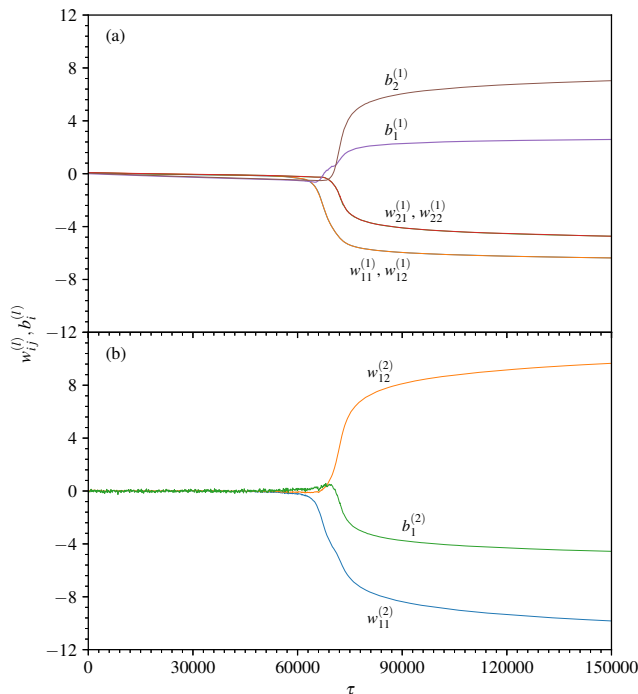


FIG. 3. Drifts of weights and biases for the (a) hidden and (b) output layer as the optimization process progresses through the epochs τ at learning rate $\eta = 0.1$. Note that the pairs of weights $w_{11}^{(1)}, w_{12}^{(1)}$ and $w_{21}^{(1)}, w_{22}^{(1)}$, respectively, are indistinguishable for this solution (#1 in Table II) of the problem.

the individual weights and biases shown in Fig. 3, we see that, after an extensive initial phase with little change, a sudden separation sets in at the same time when the loss rapidly drops (see Fig. 2). First, the weights of hidden neuron 1 start changing, which triggers a similar drop in the weight $w_{11}^{(2)}$ connecting this hidden neuron with the output neuron. In consequence, also the bias of hidden neuron 1, $b_1^{(1)}$, shifts to higher values. Only then, in a second step, all other weights and biases respond accordingly, ultimately leading to the drop of the loss and its convergence toward zero. However, even though this is achieved after about 80000 epochs, the parameters keep changing monotonously.

It is worth noting that the Adam optimizer [22] yields qualitatively the same results. The convergence sequence for the individual parameters is identical to that shown in Fig. 3. However, as expected, Adam is more efficient than stochastic gradient descent based on fixed learning rates. Convergence sets in much faster.

Despite the parameter drifts, the activation of the output, $a_1^{(2)}$, reliably converges to the expected result in each of the four cases, as is shown in Fig. 4 for backpropagation at $\eta = 0.1$. In early epochs, it fluctuates about 0.5, but only when the activations of the intermediate layer, $a_1^{(1)}$ and $a_2^{(1)}$, desync in a symmetry breaking process, $a_1^{(2)}$ can ultimately enter its convergence channel. Some-

what surprising are the rapid turns of $a_2^{(1)}$ after separating from $a_1^{(1)}$ at $\tau \approx 70000$ in the cases (0,0), (0,1), and (1,0), which initiate the transition process. The case (1,1) is special insofar as the dynamics of $a_1^{(2)}$ embarked into the wrong channel and only after an additional fluctuation in $a_2^{(1)}$ it corrects the direction and the output value eventually approaches zero. It is the distinct split in the respective dynamics of $a_1^{(1)}$ and $a_2^{(1)}$ that make this neural network find a solution to the XOR problem; a single intermediate neuron as in a perceptron representation would not have been sufficient to drive the behavior of the output neuron correctly.

It should be noted that the similar activation values in all cases at about 0.5 in the first phase are a consequence of the small initial values of the parameters randomly chosen in the interval (0,0.1); the argument of the sigmoid function at the output is close to 0 and $\sigma(0) = 0.5$. The advantage of this initialization is that convergence dynamics is well-behaved.

In order to better understand the approach to the solution, let us have a look at the convergence dynamics if one parameter is shifted away from its optimal value, whereas the other eight are kept constant at their optimal values. This is done for each weight and bias separately. The results are shown in Fig. 5. Epoch of convergence τ_{conv} is defined as the number of epochs it takes for the network to converge to solution #1 in Tab. II if one specific parameter is initialized at $[w_{ij}^{(l)}]_{\text{init}} = [w_{ij}^{(l)}]_{\text{opt}} + \Delta w_{ij}^{(l)}$ (weights) or $[b_i^{(l)}]_{\text{init}} = [b_i^{(l)}]_{\text{opt}} + \Delta b_i^{(l)}$ (biases), respectively. Convergence is achieved once the loss, averaged over up to 100 backpropagation runs with the same parameter initializations (different seeds of the random number generator generate different random batches, though), falls below the threshold value 0.005, and a test with the nonrandomized batch also yields a loss value below this threshold. This ensures that the network has indeed converged.

The results are quite remarkable and give us first clues regarding prominent features of the loss landscape. First of all, we observe that all curves possess a plateau in the vicinity of their optimal values (i.e., around zero for the shifted weights and biases). Whereas fast convergence is expected very close to the zero point, the rather large extension of the plateau for positive and negative deviations from the optimal value is rather surprising. Imagining a higher-dimensional loss landscape, this would mean that the optimal solutions are embedded in a region with almost zero loss value. We can also see that the more the selected initial weight or bias is shifted away from its optimal value the more rapidly the convergence dynamics changes. There are interesting exceptions, though. Below certain threshold values, the variation of the initial settings of the weights $w_{11}^{(1)}$, $w_{12}^{(1)}$, and $w_{11}^{(2)}$ do not affect the solution at all. From Fig. 5(a), we find that the convergence dynamics of the network is not altered

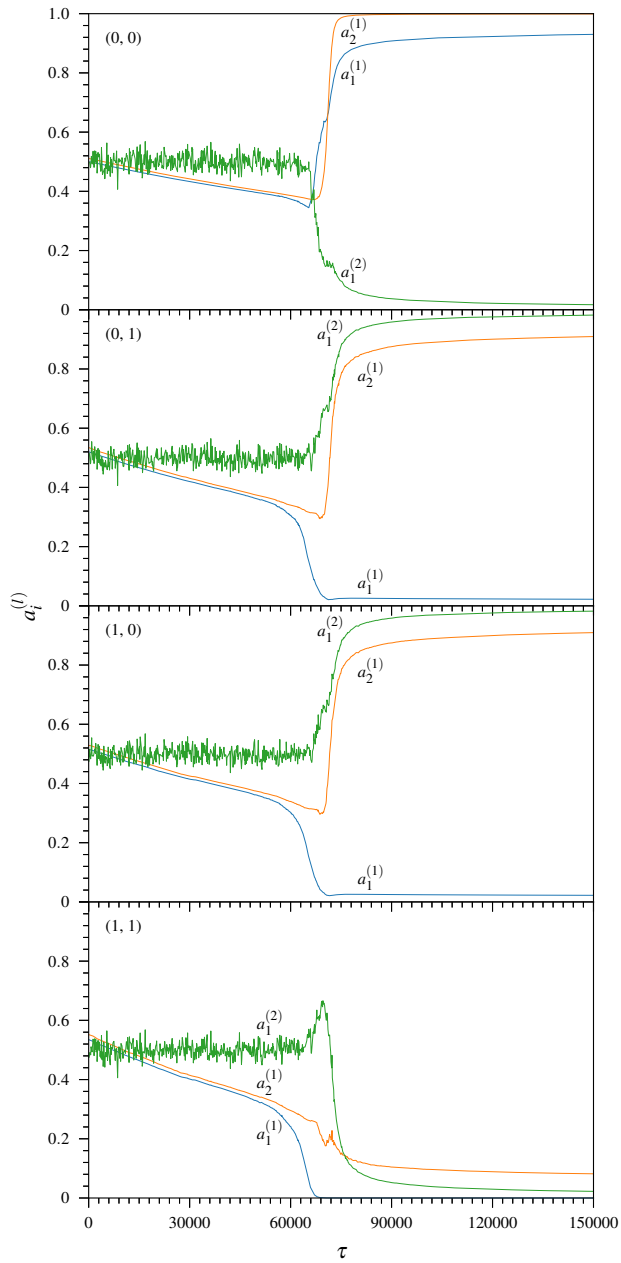


FIG. 4. Convergence of activations $a_i^{(l)}$ of hidden and output neurons to solution #1 in Table II for all four cases listed in Table I as functions of epoch τ for the XOR sigmoid network. The learning rate was $\eta = 0.1$.

if $\Delta w_{11}^{(1)} < 2.2$, $\Delta w_{12}^{(1)} < 2.2$, or $\Delta w_{11}^{(2)} < 1.6$ (provided in each case all other parameters are initialized at their optimal values). This supports the conclusion that there is indeed a continuous space of solutions, forming a valley or channel in the loss landscape.

Furthermore, it can be seen that for some of the parameter shifts convergence is slower, but remains fairly constant upon alterations of the shifts away from the optimal values. This hints at plateaus at higher loss values

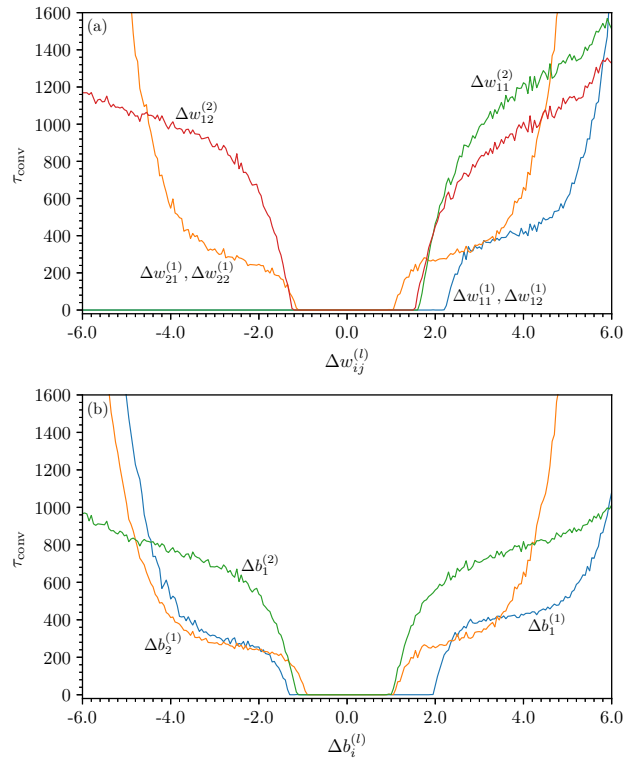


FIG. 5. Epoch of convergence τ_{conv} plotted as function of the deviation of initial (a) weights $w_{ij}^{(l)}$ and (b) biases $b_i^{(l)}$ from the respective optimal values for solution #1 given in Table II. In each case, all other weights and biases are initialized at their optimal values.

in the loss landscape.

C. Analysis of the Loss Landscape

In the following, we investigate the features of cross-sections through the loss landscape. For this purpose, we compare the results obtained by using full nonrandomized and randomized batches for the calculation of the loss in forward passes.

1. Nonrandomized Batch

The loss was defined in Eq. (4) as an average of the square deviations of the actual from the expected output values over the batch of all input cases for any given set of parameter values. Therefore, the loss function depends on all parameters and can be interpreted as a landscape in this embedding space. For the network we chose, the parameter space is nine-dimensional. In order to visualize some of its features, we have calculated all 36 cross-sections in which 7 of the 9 parameters are kept constant at their optimal values according to solution #1 in Table II, whereas two are varied about their optimal

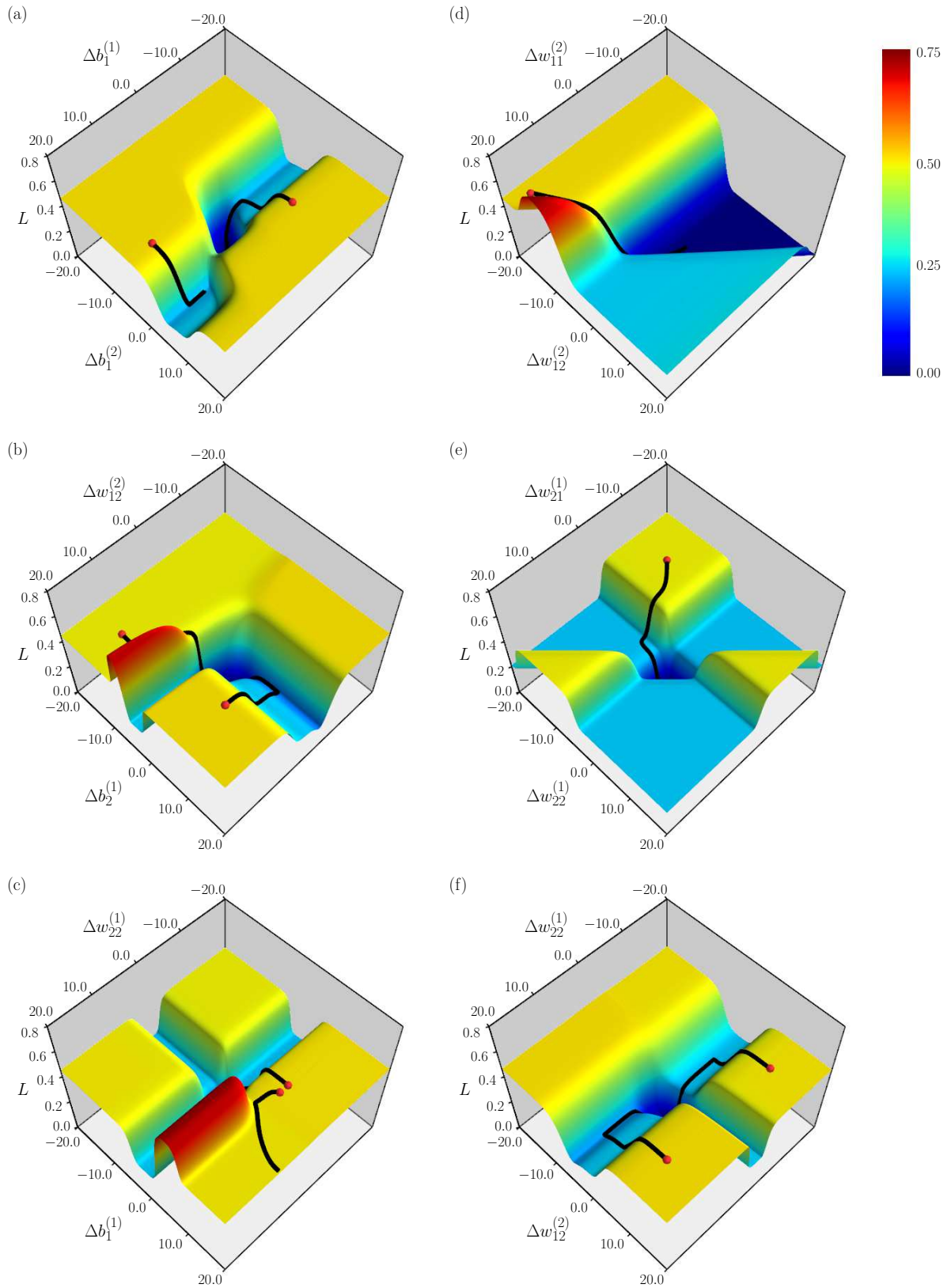


FIG. 6. Selected cross-sections of the loss landscape through the nine-dimensional parameter space. Seven parameters are kept constant at their optimal values, and two are varied about their respective optima in the ranges shown. Various trajectories are included to visualize the backpropagation dynamics starting from the locations marked by the red dots.

values in a rather large range. Cross-sections for six different choices of variable parameter pairs are shown in Fig. 6. Whereas all 36 cross-sections significantly differ from each other, the selection already contains the most distinct features. It should also be noted that, not surprisingly, landscapes look different for other solutions listed in Table II, but the cross-sections possess similar main features like the ones shown in Fig. 6. Also included in the figures are exemplified backpropagation or convergence trajectories with randomly chosen starting points. Like for the loss landscape, the complete batch of the four cases listed in Table I without randomization was used for the calculation of the trajectories and the steepest-descent method was only applied to the two variable parameters, whereas the other seven were kept strictly constant at their optimal values.

The most striking features in all figures are the channels, plateaus, and isolated rims and wells at loss values between 0 and 1 at 0.25 increments, separated by steep slopes. The prominent loss values of these features can be readily explained: According to our definition of the loss as the sum of square deviations over the full batch as used in the construction of the landscapes, zero loss can only be achieved if all outputs calculated by the network coincide exactly with their expected values in all cases. In all cross-sections shown in Fig. 6, this point is located at $(0, 0)$, and regions with values close to zero are colored dark blue. An isolated well surrounding this point is present in all cross-sections shown, except in Fig. 6(d), where the zero-loss point is at the corner of a shallow triangular, almost plateau-like, region. In Fig. 6(b), there appears to be a deep trench (also dark blue) with very small loss values converging to the zero-loss point. Such a trench, albeit at higher loss values, is also visible in Fig. 6(f).

Loss values ~ 0.25 can typically be attributed to situations, where the XOR logic of one case in the batch is determined wrongly (the output is either 1 instead of 0, or vice versa). Those regions in the landscapes are shaded turquoise. It is noticeable that these regions often form straight channels, but also plateaus.

If among the four cases in the batch two outputs are correct and two wrong, the loss value is 0.5. This is the “highest-entropy” situation as there are 6 possible combinations of pairs of cases in the batch that lead to $L = 0.5$. Consequently, there are significantly more parameter combinations representing this scenario than any other, and therefore the yellow plateaus associated with loss values around 0.5 dominate in all figures. In contrast, larger loss values are clearly suppressed in the parameter ranges plotted. Only in Figs. 6(b)–6(d), we see red-shaded rims with values at about $L = 0.75$, in which situation three cases in the batch are evaluated wrongly. Areas with even higher loss values are not present in the parameter spaces covered in any of the cross-sections analyzed in the vicinity of the optimal parameter settings. It should be noted that all real loss values between 0 and 1 are permitted as the sigmoid output is continu-

ous, but near the optimal solution, only these distinct, almost discrete, shapes of the cross-sections through the loss landscape are observed. However, for a problem with more than four cases in the full batch, the landscape features are certainly more diverse. Note that thanks to the sigmoid activations, all plateaus, channels, and trenches have slight slopes, i.e., there is always a gradient toward lower loss values leading to a local minimum at loss values larger than zero or a global minimum at zero loss.

Taking a closer look at selected convergence trajectories is quite revealing. These paths are inserted into the plots shown in Fig. 6. Since in this consideration the complete nonrandomized batch is used and not a stochastic one, the trajectories are smooth. The locations marked in red define the starting points or initial conditions for the dynamics. The learning rate was set to $\eta = 0.1$ in most cases (larger values were used where the dynamics was too slow). The simulation was stopped once convergence to zero loss was achieved or preset limits of up to 60 million epochs were reached otherwise.

Figure 6(a) contains two different trajectories. The path beginning at $(\Delta b_1^{(1)}, \Delta b_1^{(2)}) = (-7.4, 8.9)$ with loss value $L \approx 0.5$ rapidly reaches the cliff and drops to the lower level at about $L \approx 0.25$. After residing there for a number of epochs it quickly descends to the bottom and converges to the zero-loss point in the well. This is the common scenario of convergence to the optimal solution.

The behavior is completely different for the path initiated at $(\Delta b_1^{(1)}, \Delta b_1^{(2)}) = (15.0, -2.0)$ (the loss value is $L \approx 0.5$), which represents an unsuccessful attempt. It also rapidly drops to a trench at $L \approx 0.25$, but any further convergence is clearly prevented by a barrier separating this channel from the well. The path gets stuck at a local minimum. It is somewhat surprising that the loss landscape of this simple network we study here exhibits such features of complexity and is a reminder that optimization is not a straightforward process.

In Fig. 6(b), the trajectory initialized at $(\Delta w_{12}^{(2)}, \Delta b_2^{(1)}) = (12.5, -12.5)$, for which $L \approx 0.48$, contrasts the behavior described in the previous case. The origin of the path is deliberately chosen to be located behind a barrier, but the gradients are favorable and enable the “walker” to pass by the ridge and directly drop into the basin of convergence to zero loss.

Another very interesting scenario is shown in Fig. 6(c). Two trajectories are initialized in close proximity from each other, $(\Delta w_{22}^{(1)}, \Delta b_1^{(1)}) = (-5.0, 10.0)$ vs. $(-3.0, 10.0)$, both at loss values very close to $L = 0.5$. Whereas the former rapidly converges to the optimum point, the other takes a turn, hits a barrier and is diverted away from the zero-loss attraction basin. Millions of epochs later it still had not converged to this or any other solution. It seems the trajectory got trapped in a local minimum at a loss values just below $L \approx 0.5$. This divergence in the dynamics of backpropagation for this system may hint at potentially chaotic behavior in larger networks as land-

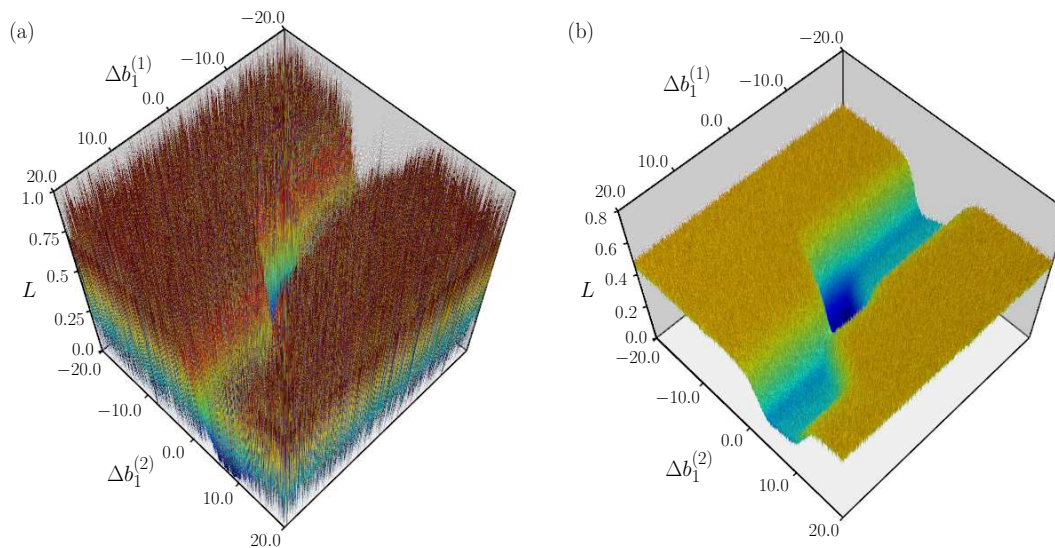


FIG. 7. Cross-section through the loss landscape with $b_1^{(1)}$ and $b_1^{(2)}$ variable for randomized batches: (a) single run, (b) average over 100 runs. Compare with the result obtained for the nonrandomized batch in Fig. 6(a).

scape shapes are more fragmented. Note that there is no stochastic component in the way we backpropagate here. At any given location, trajectories follow the steepest descent and cannot climb uphill.

2. Randomized Batches

Randomized batches are typically used for the learning process of large neural networks, where working with the full batch is not economical. It is a necessity if mini-batches are used. In this section, we again use the full batch, but with randomized cases, to determine cross-sections through the loss landscape. Since the results strongly fluctuate due to the stochastic sampling of the batch compositions, the loss landscape looks fuzzy for a single scan. This is shown in Fig. 7(a) for the cross-section, where $b_1^{(1)}$ and $b_1^{(2)}$ are variable and all other parameters are kept constant at their optimal values, according to solution #1 in Table II. Compare this to the smooth cross-section plotted in Fig. 6(a), which was obtained using the nonrandomized batch. It is interesting that, despite the strong fluctuations, the main landscape features are already visible. After averaging over 100 different scans [see Fig. 7(b)], we find that the landscape shape indeed converges to the result we obtained for the nonrandomized batch. This is reassuring as it confirms that the randomization of batches is a viable option and does not alter the basic landscape features including the attraction basin toward the optimal solution.

D. Density of Loss and Microcanonical Entropy

In modern statistical physics, the density of states $g(E)$ is often used for the identification of significant thermodynamic features such as phase transitions in complex physical systems. If \mathbf{X} is the phase space vector of all degrees of freedom (such as coordinates and momenta in Hamiltonian systems), it is defined as

$$g(E) = \int \mathcal{D}\mathbf{X} \delta(H(\mathbf{X}) - E), \quad (8)$$

where H is the energy function or Hamiltonian assigning the state \mathbf{X} an energy value, and $\mathcal{D}\mathbf{X}$ symbolizes the multi-dimensional integral measure in the state space. The integral over the Dirac δ distribution therefore counts how many states share the energy E . Since $g(E)$ addresses all states available in the phase space of the system, it can be interpreted as the phase space volume per energy unit and therefore allows for the introduction of the so-called microcanonical or restricted entropy according to Boltzmann's formula:

$$S(E) = k_B \ln g(E), \quad (9)$$

where k_B is the Boltzmann constant. This relation is the foundation of statistical physics and connects it to thermodynamics. As the system behavior is governed by the competition of enhancing entropy and reducing energy, which for most systems leads to stable thermodynamic equilibrium phases, Eq. (9) contains all information about the phase transitions a system may experience. Since the inverse temperature is defined as $\beta(E) = dS/dE$, curvature properties of $S(E)$ even allow for the identification of transition temperatures. The recently introduced generalized microcanonical inflection-

point analysis method [14] enables the systematic identification and classification of all phase transitions. It can even be used for finite systems, where the hypothetical thermodynamic limit needed in the conventional theory of phase transitions cannot be employed.

In this context, we may consider a neural network a complex physical system and interpret the learning process as a cascade of phase transitions. This can even be done for the simple artificial neural network discussed in this paper. We replace the energy by the loss and redefine $g(L)$ as the density of loss. Then $S(L) = \ln g(L)$ is a dimensionless microcanonical entropy for this problem. The shape of this curve should encode the information about the activation steps needed in the learning process to overcome the transition barriers (if there are any) toward the accomplishment of the learning objective. In this sense, learning is an annealing process passing through different phases from high-entropy states (high temperature) to the optimal solution, which represents a low-energy state (as temperature approaches zero).

Another advantage of this approach is that it covers the entire state space, but S is only a function of a single variable, L . This reduces the effort of trying to find features of the loss landscape by means of cross-sections, as done in the previous sections, dimensional reduction or the introduction of specific order parameters.

Microcanonical entropies for networks with n_h neurons in the hidden layer, obtained by generalized-ensemble Monte Carlo simulations [23–26], are shown in Fig. 8. From the curve for $n_h = 1$ it is obvious why the perceptron fails solving the XOR problem: There are simply no zero-loss states in the parameter space. For networks with two and more hidden neurons, multiple sets of parameter values for zero loss can be found. The entropy is largest around $L = 0.5$ and noticeable peaks are also found at $L = 0, 0.25, 0.75,$ and 1.0 . This is expected from the discussion of the cross-sections through the loss landscape in the previous sections. Despite the expectation of an enhanced entropy at these specific values from the discussion of the loss landscape, the very strong suppression of loss values in-between is, however, astonishing and responsible for the general complexity of the learning process. The entropy curves for networks with smaller hidden layer show additional minor peaks. These correspond to intermediate plateaus in the loss landscape and effectively slow down the optimization process. Even though adding neurons to the hidden layer significantly increases the dimension of the parameter space, these extra dimensions enable the optimizer to bypass these entropic barriers. Therefore, larger networks can improve the learning efficiency. As Fig. 8 clearly shows, these entropic “finite-size” effects gradually disappear as the number of hidden neurons is increased. This supports a virtually barrier-free learning process in larger networks [27]. This can be essential for large-scale problems, where the optimization usually starts from larger loss values. However, for the small, discrete problem studied here, no obvious benefits

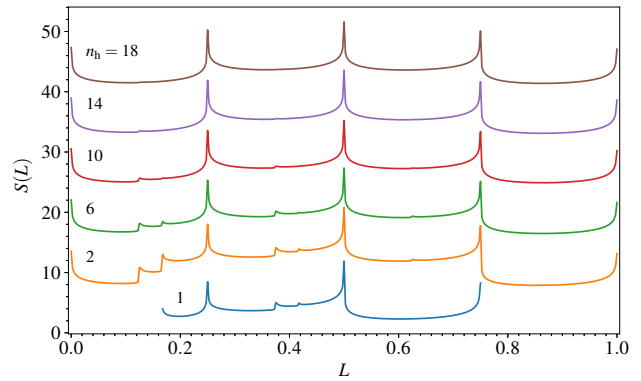


FIG. 8. Microcanonical entropies $S(L)$ for XOR networks with different numbers of neurons in the hidden layer, n_h . The curves have been shifted relative to each other vertically for better visibility.

from the smoothing of the entropy curves for the larger networks were observed in this phase of the learning process (cf. comparison for $n_h = 2$ and 18 at $\eta = 0.1$ in Fig. 2).

In the context of thermodynamic phase transitions, convex regions of the microcanonical entropy indicate first-order phase transitions [14, 16, 28]. In thermodynamic systems, first-order transitions are associated with latent heat, i.e., additional energy needed to overcome attractive interactions that keep particles bound to each other. In this dissolution process, the temperature remains unchanged, thereby slowing down any annealing process. It does not seem far fetched to adopt this interpretation here and make the convex entropy regions responsible for the slowing-down of the learning processes in neural networks, artificial and real. It will be an intriguing future task to investigate larger networks (large input data sets or number of cases and therefore possessing a network state space of much higher dimensionality) in this respect. The expectation is that the peaks and thus also the negative-slope sections in the convex regions of the entropy curve deteriorate. Negative slopes correspond to negative microcanonical temperatures and represent unstable non-equilibrium behavior in physical systems. Entropy curves for larger networks should therefore look smoother and their curvatures may encode inflection points in higher-order derivatives indicating transitions higher than first order. The reason for these assumptions is that an artificial neural network can serve as a model for a real neural network. Therefore, statistical properties of larger artificial neural networks are expected to closely resemble features of complex physical systems.

IV. SUMMARY

Understanding the dynamics of optimization processes for artificial neural networks and identifying structural properties in the loss landscape that either accelerate or decelerate the training process should be considered a key task in helping develop fields of machine learning and artificial intelligence more systematically. In this paper, we have studied aspects associated with this problem for a very simple sigmoidal neural network that represents the XOR logic with a two-bit input and single output. An analysis of the convergence dynamics showed that for fixed learning rate, network parameters need to correlate cooperatively in order to correctly activate neurons. We also found that, whereas convergence toward the solution (i.e., zero loss) is achieved, weights and biases keep drifting and, by themselves, do not converge at all, which was unexpected. This behavior can be explained by the long-term behavior of the optimization process, which exhibits a power-law decay with a characteristic exponent, which is independent of the learning rate, but depends on the number of hidden neurons. Ultimately, these network properties result in a loss landscape with distinct properties.

Investigating cross-sections through this landscape, we noticed that in the vicinity of the optimum, characteristic features like wells, channels, trenches, barriers, plateaus, and rims dominate. These geometric shapes significantly impact the convergence dynamics of the backpropagation optimization method we employed to find optimal solutions. The study as to how far these features connect to each other in the full high-dimensional parameter space is left to future work. Also, the shape of the loss landscape depends on other factors as well, e.g., the choice of the activation function. Whereas simpler activation functions than the sigmoid function used in this study may reduce computational cost in the forward pass, the optimization could be negatively affected by other types of landscape barriers. For example, our tests with ReLU activation have shown that successful convergence much more sensitively depends on the initial parameter settings and learning rates than it was in the case of sigmoid ac-

tivation. We also investigated potential impacts of non-randomized and randomized full batches of input data on the landscape features and found that the landscape features obtained by averages over randomized batches resemble those obtained from the forward passes of the nonrandomized batch. Randomization, which is a necessity when using mini-batches for large data sets, may even accelerate the annealing process in the search for the optimal solution.

Eventually, we introduced the microcanonical entropy of neural networks as the logarithm of the density of loss as a variant of the density of states that commonly aids the understanding of the statistical physics of phase transitions in thermodynamic systems. Comparing entropy curves for networks with different numbers of hidden neurons reveals the disappearance of smaller entropic barriers, which indeed supports earlier claims that optimization processes in neural networks are essentially barrier-free [27]. The analysis of curvature features of microcanonical entropy curves has turned out to be very useful in the identification and classification of phase transitions in physical systems [14]. Transferring this idea to neural networks, different stages of learning success represent stable phases. Rapid, low-entropy drops in the loss landscape can then be understood as phase transitions accompanying the learning process. Approaching zero loss is equivalent to cooling down a macroscopic system, i.e., entering more and more ordered phases with lower entropy until, ultimately, the ground state is reached. The results obtained in this simple case study are already intriguing and may encourage more generalized analyses for larger networks. The identification of virtual, effective parameters for the representation of the loss landscape may help guide network training processes more efficiently.

ACKNOWLEDGMENTS

KA thanks the Center for Simulation Physics at UGA for hospitality and support.

-
- [1] H. J. Kelley, *ARS Journal* **30**, 947 (1960).
 - [2] A. E. Bryson, *A gradient method for optimizing multi-stage allocation processes*, in: *Proc. Harvard Symposium on Digital Computers and Their Applications* (1962).
 - [3] D. E. Rumelhart, G. E. Hinton, and R. J. Williams, *Nature* **323**, 533 (1986).
 - [4] P. Werbos, *Proc. IEEE* **78**, 1550 (1990).
 - [5] S. Russell and P. Norvig, *Artificial Intelligence: A Modern Approach*, Fourth Edition (Pearson, 2022).
 - [6] F. Rosenblatt, *Psychol. Rev.* **65**, 386 (1958).
 - [7] M. L. Minsky and S. A. Papert, *Perceptrons* (MIT Press, Cambridge, MA, USA, 1969).
 - [8] D. E. Rumelhart, G. E. Hinton, and R. J. Williams, *Learning Internal Representations by Error Propagation*, in: *Parallel Distributed Processing, Volume 1: Explorations in the Microstructure of Cognition: Foundations*, ed. by D. E. Rumelhart, J. L. McClelland, and the PDP Research Group (MIT Press, Boston MA, 1986), pp. 318.
 - [9] E. Herberg, e-print: arXiv:2304.05133 (2023).
 - [10] J. J. Hopfield, *Proc. Nat. Acad. Sci. (USA)* **79**, 2554 (1982).
 - [11] T. Poggio, A. Banburskia, and Q. Liaoa, *Proc. Nat. Acad. Sci. (USA)* **117**, 30039 (2020).
 - [12] M. Gori, R. Franzosi, G. Pettini, and M. Pettini, *J. Phys. A: Math. Theor.* **55**, 375002 (2022).

- [13] L. Di Cairano, *J. Phys. A: Math. Theor.* **55**, 27LT01 (2022).
- [14] K. Qi and M. Bachmann, *Phys. Rev. Lett.* **120**, 180601 (2018).
- [15] D. Aierken and M. Bachmann, *PCCP* **25**, 30246 (2023).
- [16] M. Bachmann, *Thermodynamics and Statistical Mechanics of Macromolecular Systems* (Cambridge University Press, Cambridge UK, 2014).
- [17] A. J. Ballard, R. Das, S. Martiniani, D. Mehta, L. Sagun, J. D. Stevenson, and D. J. Wales, *Phys. Chem. Chem. Phys.* **19**, 12585 (2017).
- [18] D. Mehta, X. Zhao, E. A. Bernal, and D. J. Wales, *Phys. Rev. E* **97**, 052307 (2018).
- [19] H. Li, Z. Xu, G. Taylor, C. Studer, and T. Goldstein, *arXiv:1712.09913* (2018).
- [20] *Mathematical Aspects of Deep Learning*, ed. by P. Grohs and G. Kutyniok (Cambridge University Press, Cambridge UK, 2022).
- [21] S. Whitelam, V. Selin, I. Benlolo, C. Casert, and I. Tamlyn, *arXiv:2205.07408* (2022).
- [22] D. P. Kingma and J. L. Ba, *Adam: A Method for Stochastic Optimization*, in: Proceedings of the 3rd International Conference on Learning Representations (ICLR 2015), San Diego, CA, USA, May 7-9, 2015, ed. by Y. Bengio and Y. LeCun; e-print: *arXiv:1412.6980* (2014).
- [23] F. Wang and D. P. Landau, *Phys. Rev. Lett.* **86**, 2050 (2001).
- [24] F. Wang and D. P. Landau, *Phys. Rev. E* **64**, 056101 (2001).
- [25] B. A. Berg and T. Neuhaus, *Phys. Lett. B* **267**, 249 (1991).
- [26] B. A. Berg and T. Neuhaus, *Phys. Rev. Lett.* **68**, 9 (1992).
- [27] F. Draxler, K. Veschgini, M. Salmhofer, and F. Hamprecht, *Essentially No Barriers in Neural Network Energy Landscape*, in: Proceedings of the 35th International Conference on Machine Learning, PMLR **80**, 1309 (2018).
- [28] D. H. E. Gross, *Microcanonical Thermodynamics: Phase Transitions in "Small" Systems* (World Scientific, Singapore, 2001).